Editor
Timothy P. Hanusa

The Lightest Metals

Science and Technology from Lithium to Calcium

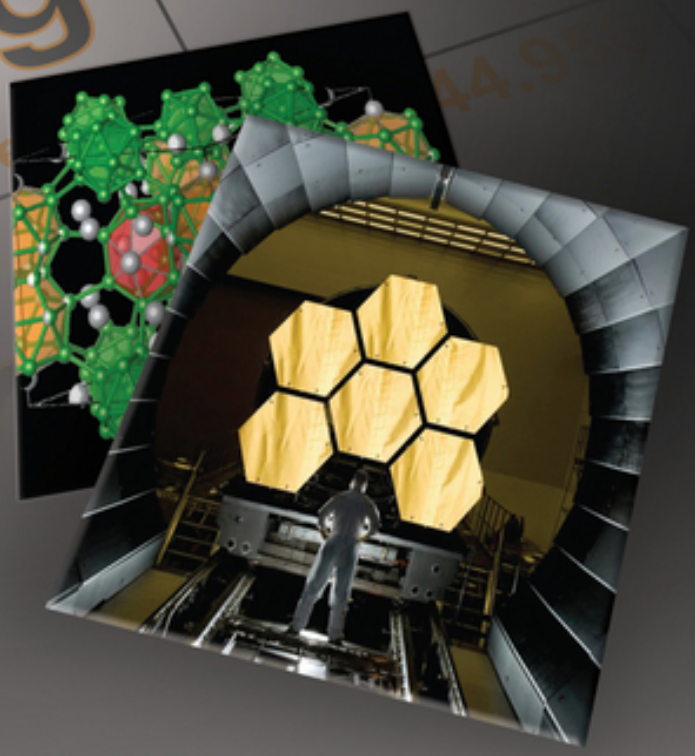

Encyclopedia of Inorganic and Bioinorganic Chemistry

Visit the online Encyclopedia of Inorganic and Bioinorganic Chemistry at **www.wileyonlinelibrary.com/ref/eibc**

WILEY

Table of Contents

List of Illustrations

Occurrence and Production of Beryllium

Solution NMR of the Light Main Group Metals

Solid-State NMR of the Light Main Group Metals

Figure 5 (a) Analytical simulation of a ^{23}Na (I = 3/2) powder pattern simulated with a C_Q = 200 kHz and η_Q = 0 under static conditions (i.e., ν_{rot} = 0 kHz). (b) Schematic representation of the powder patterns arising from the central transition and the overlapping satellite transitions, which are commonly observed for half-integer quadrupolar nuclei possessing small values of C_Q

Figure 6 Analytical simulations of a ^{35}Cl (I = 3/2) central-transition powder pattern simulated at 9.4 T with a C_Q = 4.0 MHz and η_Q = 0 under (a) static conditions and (b) magic-angle spinning

Figure 7 Euler angles (α, β, γ) relating the principal axis systems of the EFG and CS tensors

Figure 8 (a) Schematic representation of magic-angle spinning showing the rotor oriented at 54.74° with respect to the external magnetic field. (b) NMR spectra acquired under static and spinning conditions. Two spinning speeds are used to identify the isotropic chemical shift

Figure 9 Analytical simulations of static ^{35}Cl central-transition powder patterns at 9.4 T with (a) C_Q = 4.0 MHz and η_Q ranging from 0.2 to 1 and (b) η_Q = 0 and C_Q ranging from 1.0 to 4.0 MHz. The positions of the discontinuities resulting from η_Q and the broadening of the powder pattern due to the increased value of C_Q are shown

Figure 10 (a) Schematic representation of the two-dimensional DAS experiment which averages the first- and second-order quadrupolar interactions by sequentially spinning at angles of 37° and 79° with respect to $\mathbf{B}_0$ during the t_1 evolution period. The

rotor is flipped to the magic-angle during the t_2 period for spectral acquisition. (Adapted with permission from Ref. [18] (© Elsevier, 2005) and Ref. [19] (© Wiley-VCH, 2004)) (b) Schematic representation of the double-rotor design used in DOR to average the first- and second-order quadrupolar interactions by simultaneously spinning at angles of 30.56° and 54.74° (Adapted with permission from Ref. [10]. © Wiley-VCH, 2006)

Figure 11 (a) Schematic representation of the two-pulse multiple-quantum MAS (MQMAS) pulse sequence and the coherence transfer pathway diagram for a triple-quantum (3Q) MAS experiment. (b) Schematic representation of the satellite-transition MAS (STMAS) pulse sequence and coherence transfer pathway diagram (Adapted with permission from Ref. [10]. © Wiley-VCH, 2006)

Figure 12 Schematic representations of the (a) CPMG, (b) WCPMG, and (c) BRAIN-CP/WURST-CPMG pulse sequences

Figure 13 (a) The SEDOR pulse sequence. The SEDOR fraction is the reduction in the echo intensity with respect to that obtained without irradiating the *S* spin. (b) The REDOR pulse sequence. All rectangular pulses are π pulses (unless indicated otherwise). (c) The TRAPDOR pulse sequence. A rotor-synchronized spin-echo is applied to the ^{1}H spins whilst the quadrupolar spins are irradiated during the defocusing and/or refocusing times. The TRAPDOR fraction is obtained by comparing the reduction in spin-echo intensity to that obtained without irradiation. (d) The REAPDOR pulse sequence. The phases of the π pulses are indicated

Figure 14 Two-dimensional pure-absorption exchange NMR spectra of Li_4SiO_4 acquired at 33 °C using mixing times of (a) 47 ms and (b) 188 ms. The coordination numbers for the Li sites and the exchange peaks are indicated. The horizontal axis is the direct dimension

Figure 15 ^{6}Li MAS NMR spectra of (a) $Li_2Mn_4O_9$, (b) $Li_4Mn_5O_{12}$, and (c) $Li_2Mn_2O_4$ acquired with spinning speeds of around 21 and 9 kHz for [(a) and (b)] and (c), respectively. The isotropic shifts of paramagnetic phases are labeled

Figure 16 (a) ^{6}Li MAS NMR spectrum (ν_0 = 116.6 MHz) and (b) ^{7}Li MAS NMR spectrum (ν_0 = 44.2 MHz) of LiX-1.25. (c) Schematic diagram of cation positions in faujasite

Figure 17 ^{7}Li static NMR powder patterns for (a) triphenylmethyllithiumquinuclidine (dominating quadrupolar interaction), (b) lithiocene-P(C_6H_5)$_4$ (dominating chemical shift anisotropy), and (c) *o*,*o*-(TMEDA)$_2$ (strong homonuclear ^{7}Li-^{7}Li dipolar coupling)

Figure 18 ^{1}H-^{6}Li CP NMR spectrum of 2,4,6-tri(isopropyl)phenyllithium acquired under static conditions

Figure 19 Relationship between the magnitude of C_Q and the molecular site symmetry for ^{23}Na nuclides in Na atoms coordinated to oxygens

Figure 20 ^{23}Na triple quantum MAS NMR spectra of (a) 2HFC-134/NaX and (b) fully loaded HFC-134/NaX after applying the shearing transformation. Asterisks

Figure 26 ^{27}Al NMR spectra of MgO(3.5Al_2O_3) spinel acquired under (a) static and (b) MAS conditions and ^{27}Al MAS spectra of (c) α-Al_2O_3, (d) Na-Y zeolite, and (e) AIN. All spectra were acquired at 9.4 T

Figure 27 (a) ^{27}Al static and MAS CT NMR spectra of Al_3Ti. (b) Expansion of the MAS spectrum in (a) with accompanying simulation (shown below and above, respectively). (c) ^{27}Al static spectrum of Al_3Ti showing the overlapping satellite (±1/2 ↔ ±3/2 and ±3/2 ↔ ±5/2) line shapes. Resonances corresponding to metallic aluminum are denoted with * and † in (b) and (c), respectively

Figure 28 3Q-D-HETCOR (3Q = triple quantum; D = dipolar correlation) NMR spectrum (left) of aluminophosphate $AlPO_4$-14 showing the correlations of tetrahedral and five-coordinated aluminum sites with phosphorus. The ^{31}P skyline projections are shown above the spectrum, which were observed (a) without and (b) with SPAM. The total acquisition time was 20 h. (c) ^{27}Al-^{29}Si D-HETCOR, and (d) ^{27}Al-^{29}Si SPAM-3Q-D-HETCOR NMR spectra of microcline. The 1D ^{29}SI MAS spectrum is shown for comparison on top of (c). The total acquisition times were 80 and 72 h for (c) and (d), respectively. All spectra were acquired at 9.4 T

Figure 29 ^{27}Al MQMAS NMR spectrum of steamed zeolite β, (H)β1 550(3d)w30. Peaks corresponding to three tetrahedral aluminums ($Al(IV)_a$, $Al(IV)_b$, and $Al(IV)_c$) and two octahedral aluminums ($Al(VI)_a$ and $Al(VI)_b$) are visible. The ^{27}Al MAS NMR spectrum is presented on top of the MQMAS spectrum

Figure 30 ^{27}Al MAS NMR spectra of super-quenched glass samples showing peaks corresponding to 4-, 5-, and 6-coordinate Al sites, and spectra of non-quenched sample only showing peaks corresponding to 4- and 6-coordinate sites. The sample compositions are indicated for each spectrum in mol % with SiO_2 and Al_2O_3 denoted by S and A, respectively. All spectra were acquired with a spinning speed of around 15 kHz

Figure 31 Frequency-stepped ^{27}Al CPMG NMR spectra of (a) $AlMes_3$ and (b) $Al(NTMS_2)_3$. The individual sub-spectra are shown on top with the corresponding total powder pattern shown on the bottom. Co-addition was used to form the total powder pattern. † and # indicate FM radio signal interference and impurities, respectively

Figure 32 Experimental (top) and simulated (bottom) static ^{27}Al powder patterns of $[Cp^*_2Al][AlCl_4]$ collected at 9.4 T. The patterns are dominated by the effects of the aluminum CSA

Figure 33 (a) ^{39}K NMR lineshapes for alkali metal C_{60} compounds, given in order of increasing lattice constant from top to bottom. ^{39}K NMR lineshapes at several temperatures for (b) K_3C_{60}, and (c) Rb_2KC_{60}

Figure 34 ^{39}K spin-echo MAS NMR spectra for the potassium aluminosilicates. All spectra were collected at 18.8 T using a spinning speed of ca. 15 kHz. The dashed line at 0 ppm is included for reference

Figure 35 Experimental ^{39}K MAS NMR spectra collected at 19.6 T. A spinning speed of 10 kHz was

used for G1 and G2 and a spinning speed of 8 kHz was used for G3, K(2′-AMP) and K(5′-ADP)

Figure 36 Experimental ^{39}K 1D MAS and 2D MQMAS NMR spectra of (a) KPic, (b) KGP, and (c) G4 collected at 19.6 T. The spinning speed was 8 kHz in all experiments and pure absorptive 2D spectra were collected by combing SPAM with the shifted-echo method. The t_1 increment in the MQMAS experiment was rotor synchronized. The sharp signal at 0 ppm in (a) results from trace amounts of micro domains within the solid

Figure 37 A comparison of (a) ^{1}H-^{39}K BRAIN-CP/WURST-CPMG and (b) direct excitation ^{39}K DFS-QCPMG NMR spectra of potassocene (CpK) acquired at 9.4 T. The former took 128 scans and 10 min total acquisition time. The latter took 18 000 scans and 25 h total acquisition time (Schurko, 2015, unpublished data)

Figure 38 ^{25}Mg MAS NMR spectra of synthetic hydrotalcite acquired at 11.7 T. (a) unheated and heated to (b) 200 °C; (c) 300 °C; (d) 400 °C; (e) 600 °C; and (f) 1200 °C

Figure 39 Natural-abundance ^{25}Mg SPAM-3QMAS NMR spectrum of MgAl-25-NO_3^-. The dashed lines show the anisotropic slices of the three distinct Mg sites

Figure 40 Static ^{25}Mg SSNMR spectra of CPO-27-Mg as a function of rehydration degree. All spectra were acquired under identical experimental conditions. The * indicates a small amount of impurity likely resulting from magnesium oxide

Cation-π Interactions

Ion Channels and Ionophores

Aryllithiums and Hetaryllithiums: Generation and Reactivity